



Analysis of leading edge erosion effects on turbulent flow over airfoils

Akshay Koodly Ravishankara ^{a, b, *}, Huseyin Özdemir ^a, Edwin van der Weide ^b

^a TNO Energy Transition, Westerduinweg 3, 1755 LE Petten, the Netherlands

^b University of Twente, Drienerlolaan 5, 7522 NB, Enschede, the Netherlands



ARTICLE INFO

Article history:

Received 22 October 2020
 Received in revised form
 13 February 2021
 Accepted 6 March 2021
 Available online 11 March 2021

Keywords:

Leading edge erosion
 Roughness modeling
 RANS
 SU2

ABSTRACT

The surface of wind turbine blades are prone to degradation due to exposure to the elements. Rain, hail, insects are among the many causes of turbine blade degradation or erosion. Surface degradation of the wind turbine blades leads to a reduction in the aerodynamic performance, resulting in power losses. The effect of surface degradation is studied by modeling the turbine blade as a rough surface. Surface roughness can be positive (insects or other foreign objects) or negative (erosion, delamination). The individual roughness elements are however very small and it is not always feasible to study the actual degraded surface. Thus various roughness models have been proposed in the literature which eliminate the need to accurately model the degraded surface by representing erosion with a virtual surface and modeling the effect of erosion on the flow quantities near the eroded surface. In this study, the reduction in performance of airfoils due to leading edge roughness is quantified. Different roughness models are investigated and evaluated against theoretical models. Additionally, the effect of roughness on different integral boundary layer quantities like displacement thickness, momentum thickness and skin friction are presented.

© 2021 The Author(s). Published by Elsevier Ltd. This is an open access article under the CC BY license (<http://creativecommons.org/licenses/by/4.0/>).

1. Introduction

Leading edge erosion is an issue of growing concern in the wind turbine industry in recent years. The combination of growth in the size of wind turbines, increased offshore installations, especially in locations with more adverse weather conditions, has made this subject crucial to the industry [1]. Erosion of turbine blades are largely caused by rain, hailstones, accumulation of contaminants and tends to change the shape of the airfoils. This leads to a reduction in aerodynamic performance of the affected sections. Han [2] presented the effects of contamination of the airfoil used at blade tips on a 5 MW NREL turbine blade using CFD simulations. They report a worst case scenario where the Annual Energy Production (AEP) drops by 3.7%. Herring [1] presents a thorough review on the growing importance of leading edge erosion and different coating alternatives to reduce the impact of erosion. A wide range of drop in AEP, from about 25% to about 3.7%, is reported and the authors suggest it is due to different operating conditions and roughness levels used to evaluate the impact of erosion. The

authors also note that repair of moderate erosion can recover the AEP by about 2%. Keegan et al. [3] review some of the leading causes of erosion of wind turbine blades including raindrops, hailstones, exposure of composite materials to UV surfaces among others. The authors note that the increasing tip speeds of turbine blades make them increasingly vulnerable to erosion by raindrops and hailstones.

In order to quantify the adverse effects of roughness the flow around the turbine blades should be investigated. Laminar flow tends to transition to turbulent flow prematurely in presence of roughness. A review of experimental approaches to model roughness and its effect on transition can be found in Ehrmann et al. [4] Langel et al. [5] performed experiments on two airfoils by adding cut vinyl decals and focused on $100 < Re_k < 400$, where Re_k is the Reynolds number based on roughness height k . They also present a numerical approach to model the effect of roughness on transition by adding a scalar field variable. The new scalar variable is used to modify the $\gamma - Re_\theta$ transition model [6]. Sareen et al. [7] note that most of the experimental studies on roughness use strips or zigzag tapes to simulate real roughness and not many studies exist on negative roughness like erosion where material is lost from the blade.

Apart from causing early transition, the nature of the turbulent boundary layer also changes due to roughness. Skin friction

* Corresponding author. TNO Energy Transition, Westerduinweg 3, 1755 LE Petten, the Netherlands.

E-mail address: akshay.koodlyravishankara@tno.nl (A. Koodly Ravishankara).

increases and a shift in the velocity profile in the inner part of the boundary layer is observed. The additional dissipation near the roughness elements leads to thickening of the boundary layer which can make the boundary layer prone to early separation.

The concept of equivalent sand grain roughness is widely used in turbulence models to account for the effect of roughness on turbulent boundary layers. Nikuradse [8] performed experiments to measure pressure losses across pipes due to roughness, which forms the basis of the sand grain roughness concept. Nikuradse provided relations for the loss in pressure head (friction) and the velocity shift as a function of sand grain roughness heights. Real roughness is first converted to equivalent sand grain roughness when using the roughness models for Reynolds averaged Navier Stokes (RANS) turbulence models. Typically the rough surface is replaced by a smooth surface and the effect of roughness is modeled as extra dissipation in the inner boundary layer.

Integral boundary layer based tools like RFOIL [9] are used extensively in the wind energy community for quick and accurate analysis of airfoil performance, especially in combination with other methods like Blade Element Momentum theory, to obtain power output of wind turbines in a relatively inexpensive manner. However, it is restricted mainly to clean airfoils due to lack of research on developing roughness models for integral boundary layer methods. Olsen et al. [10] recently proposed a new closure relation for skin friction in the presence of roughness. The authors also note that further work is necessary to refine their study.

In this study, roughness models for SA and SST $k-\omega$ turbulence models are implemented in the open source tool SU2 [11]. The grid requirements and the accuracy of the two models are examined and validated against experimental data. Two airfoils are considered - NACA 652215 and a popular wind turbine airfoil DU-96-W-180. The NACA 652215 airfoil has been used for validating roughness models earlier [12,13]. Sareen et al. [7] performed experiments on the DU-W-96-180 with 'negative' roughness. Thus different ways to obtain equivalent sand grain roughness for 'negative' roughness are also examined in this paper. The numerical solution of the RANS equations is then used to analyze the behavior of the turbulent boundary layer and the various integral boundary layer quantities in the presence of roughness as well as to analyze the integral boundary layer parameters in order to improve roughness modeling in integral boundary layer methods.

The organization of the paper is as follows: section 2 gives information about SU2, the CFD solver used for the numerical simulations. In Section 3, two different roughness models for RANS are presented with some validation cases in section 4. Based on the results in section 4, the SA roughness model is validated against experiments on airfoils in section 5. In section 6, the effect of roughness on various integral boundary layer properties is analysed. The conclusions are presented in section 7.

2. Numerical method

2.1. SU2

SU2, the CFD solver used in this study, is an open-source collection of C++ based software tools for performing Partial Differential Equation (PDE) analysis and solving PDE-constrained optimization problems [11]. Originally developed for aerospace applications, the solver has been extended for incompressible flows [14,15]. In this study, we use the low Mach preconditioned incompressible flow solver [14]. The governing equations of SU2 solved on a domain Ω are written in the general form as

$$\frac{\partial U}{\partial t} + \frac{\partial F_i^c}{\partial x_i} - \frac{\partial F_i^v}{\partial x_i} = Q \quad \text{in } \Omega, \quad t > 0, \quad (1)$$

where U is the vector of conservative variables, F_i^c are the convective fluxes, F_i^v are the viscous fluxes and Q is a source term defined as

$$U = \begin{bmatrix} \rho \\ \rho u_i \end{bmatrix}, F_i^c = \begin{bmatrix} \rho u_i \\ \rho u_i u_j + P \delta_{ij} \end{bmatrix}, F_i^v = \begin{bmatrix} 0 \\ \tau_{ij} \end{bmatrix} \quad (2)$$

$$Q = \begin{bmatrix} 0 \\ 0 \end{bmatrix}.$$

Here u_i are the components of the velocity vector, ρ is the density, P is the dynamic pressure and the viscous stresses are $\tau_{ij} = \mu_{tot} \left(\partial_j u_i + \partial_i u_j - \frac{2}{3} \delta_{ij} \partial_k u_k \right)$. The total viscosity coefficient, μ_{tot} is the sum of the dynamic viscosity μ_{dyn} and turbulent viscosity μ_{tur} , which is computed via a turbulence model. The Spalart-Allmaras (SA) [16] and the Mean Shear Stress Transport (SST) [17] turbulence models can be used to compute μ_{tur} . More details on the low Mach number preconditioning method can be found in Ref. [14].

2.1.1. Spatial discretization

The spatial discretization is performed on an edge based dual grid using a finite volume approach. The control volumes are constructed using a median-dual (vertex-based) scheme. An upwind Flux Difference Splitting (FDS) scheme is used to compute the convective flux residual. The MUSCL scheme in combination with the van Albada slope limiter is used to obtain second order accuracy. The gradients for flux reconstruction are computed using the Weighted Least Squares method. The gradients required to evaluate the viscous fluxes are computed using either the Least Squares method or the Green Gauss theorem.

2.1.2. Time discretization

Steady state problems are also solved using a pseudo-time stepping approach where the solution is marched in time until convergence. Time integration is carried out using the Implicit Euler method.

2.1.3. Boundary conditions

For the test cases considered in this study, only the no-slip wall boundary condition on the surface of the airfoil and the far field boundary condition on the external domain is necessary. Since SU2 uses a vertex-based dual grid approach, the implementation of the no slip boundary condition is relatively straightforward. For the momentum equations, a no slip condition is enforced strongly by setting the velocity on the wall to zero (since no wall movement is necessary) and a Neumann boundary condition is used for the other equations. For the far field boundaries, the flux across the face is computed in a similar manner to internal faces where the neighboring states are assumed to be the internal solution and the free stream value.

2.2. Turbulence modeling

2.2.1. Spalart-allmaras (SA)

The SA model [16] with no trip term can be written in the general form of equation 3

$$U = \tilde{v}, \quad F_i^c = u_i \tilde{v}, \quad F_i^v = \frac{(\nu + \tilde{\nu})}{\sigma} \frac{\partial \tilde{v}}{\partial x_i} \tag{3}$$

$$Q = c_{b1} \tilde{S} \tilde{v} - c_{w1} f_w \left(\frac{\tilde{v}}{d_s} \right)^2 + \frac{c_{b2}}{\sigma} \left| \frac{\partial \tilde{v}}{\partial x_i} \right|^2$$

The turbulent viscosity is then computed as

$$\mu_{tur} = \rho \tilde{\nu} f_{v1}, \quad f_{v1} = \frac{\chi^3}{\chi^3 + c_{v1}^3}, \quad \chi = \frac{\tilde{\nu}}{\nu}$$

$$\tilde{S} = \Omega + \frac{\tilde{\nu}}{\kappa^2 d^2} f_{v2}, \quad f_{v2} = 1 - \frac{\chi}{1 + \chi f_{v1}}$$

Here $\nu = \frac{\mu}{\rho}$ is the kinematic viscosity and d is the distance to the nearest wall. The definitions of the other model constants can be found in the literature [16,18].

2.2.2. SST $k-\omega$

Following the general form of the equations in equation (1), the corresponding terms for the SST $k-\omega$ [17] model are

$$U = \begin{bmatrix} \rho k \\ \rho \omega \end{bmatrix}, F_i^c = \begin{bmatrix} \rho u_i k \\ \rho u_i \omega \end{bmatrix}, F_i^v = \begin{bmatrix} (\mu + \sigma_k \mu_t) \frac{\partial k}{\partial x_i} \\ (\mu + \sigma_\omega \mu_t) \frac{\partial \omega}{\partial x_i} \end{bmatrix} \tag{4}$$

$$Q = \begin{bmatrix} P - \beta^* \rho \omega k \\ \frac{\gamma}{\nu_t} P - \beta \rho \omega^2 + 2(1 - F_1) \frac{\rho \sigma}{\omega} \frac{\partial k}{\partial x_i} \frac{\partial \omega}{\partial x_i} \end{bmatrix}$$

Here the production term, $P = \tau_{ij} \frac{\partial u_i}{\partial x_j}$, where τ_{ij} is defined earlier in section 2.1, ρ is density, $\nu_t = \mu_t / \rho$ is the kinematic turbulent viscosity and μ is dynamic viscosity. The turbulent eddy viscosity is computed as

$$\mu_t = \frac{\rho a_1 k}{\max(a_1 \omega, \Omega F_2)} \tag{5}$$

where Ω is the vorticity magnitude and F_2 is a model constant. More information can be found in the literature [17].

2.2.3. Boundary conditions

At the far field the boundary conditions for the SA and SST $k-\omega$ model are respectively

$$\nu_{t,\infty} = 0.210438 \nu_\infty \text{ to } 1.294234 \nu_\infty,$$

$$k_\infty = (3.0/2.0) V_\infty^2 Tl^2,$$

$$\omega_\infty = \rho k_\infty / (\mu_{lam} (\mu_t / \mu_{lam})).$$

Here ν_∞ is the kinematic viscosity in the free stream, V_∞ is the free stream velocity magnitude, ρ is the density and Tl is the turbulent intensity. The ratio μ_t / μ_{lam} and turbulent intensity Tl are specified as inputs. On solid walls, the boundary conditions for clean walls are defined below.

$$\nu_t = 0,$$

$$k = 0,$$

$$\omega = 10 \frac{6\nu}{\beta_1 (\Delta d)^2}$$

Δd is the distance to the nearest normal neighbor and β_1 is a model constant. Model constant definitions can be found in the literature [11,19].

3. Roughness modeling

To motivate the roughness model used in this study, a brief introduction of turbulent boundary layers and the impact of roughness is presented below.

The turbulent boundary layer can be broadly divided into two regions [20,21]: the inner region where viscous dissipation is comparable to the turbulent dissipation and the outer region where turbulence dissipation dominates completely. The inner region can be further subdivided into three regions - the viscous sub-layer where viscous effects dominate and turbulent effects are absent, a buffer region where the turbulent stresses start to grow and finally an overlap region or a logarithmic region where the turbulent and viscous dissipation match. The overlap region leads into the outer layer of the boundary layer where viscous effects are minimal. The velocity profile in the viscous sub-layer and logarithmic region can be written respectively as

$$u^+ = y^+, \quad y^+ \leq 5, \tag{6}$$

$$u^+ = \frac{1}{\kappa} \ln(y^+) + C, \quad y^+ > 30. \tag{7}$$

The region of the boundary layer between $5 \leq y^+ \leq 30$ is the buffer region. In the above relations, y^+ is the non dimensional wall normal coordinate and u^+ is the normalized velocity defined as

$$y^+ = \frac{y u_\tau}{\nu}, \quad u^+ = \frac{u}{u_\tau}, \quad u_\tau = \sqrt{\frac{\tau_w}{\rho}}$$

Here u_τ is known as the wall friction velocity and is used as the velocity scale close to the wall, τ_w is the wall shear stress, ρ is the density, u is the local velocity and ν is the kinematic viscosity. The constant in equation (7) for a smooth wall is known to be $C = 5.0$.

The presence of surface roughness on the wall alters the nature of the velocity distribution near the wall. The roughness elements will introduce new turbulent fluctuations in the flow increasing the skin friction. Typically, a standardized notion of roughness known as the “equivalent sand grain roughness height (k_s)” is used to denote roughness of a wall [8,21,22]. A given physical roughness distribution is converted into the “equivalent sand grain roughness height” using empirical correlations like [23–25]. A more detailed review is presented in section 5.2.3. Based on the non dimensional roughness height, $k_s^+ = k_s u_\tau / \nu$, three regimes of roughness can be identified [21]. If the roughness elements are within the viscous sub-layer ($k_s^+ \leq 5$, hydraulically smooth), the effect of roughness is not relevant and there is no difference with the smooth velocity profile. As the height of the roughness element increases ($5 \leq k_s^+ \leq 70$, transitionally rough), a shift in the velocity profile is observed. Once the roughness elements are fully within the overlap region ($k_s^+ > 70$, fully rough), the viscous sub-layer plays no part and the flow is in the fully rough regime. It must be noted here that the equivalent sand grain roughness concept typically applies only to the commonly observed distributed roughness ($k-$ type roughness [26]) and not to isolated roughness elements. To reproduce the proper shift Δu^+ in the boundary layer velocity profiles, turbulence models typically increase the eddy viscosity dissipation within the inner part of the boundary layer [22]. Aupoix et al. [22], identify two methods to accomplish this with eddy viscosity based turbulence models (e.g SA and SST):

1. Finite eddy viscosity at the wall which can be interpreted as using a virtual wall to represent roughness and
2. Zero eddy viscosity at the wall where the origin of the wall is at the bottom of roughness but turbulence damping in the wall region is reduced.

With this background on roughness modeling in turbulent boundary layers, roughness models for the SA and SST turbulence models are presented.

3.1. Roughness modification for SA model

The roughness modification proposed by Boeing [18,22] is considered in this section. An alternate modification was also proposed by ONERA in Aupoix et al. [22], but is not considered since it requires the additional input of friction velocity. The effect of roughness is accounted for by shifting the virtual wall to the top of the roughness element. This can be achieved by offsetting the distance to the wall everywhere. The changes to the turbulence model are

$$d_{new} = d_{min} + 0.03k_s, \tag{8}$$

$$\chi = \frac{\tilde{\nu}}{\nu} + c_{R1} \frac{k_s}{d_{new}}, \tag{9}$$

$$f_{v2} = 1 - \frac{\tilde{\nu}}{\nu + \tilde{\nu}f_{v1}}. \tag{10}$$

with $c_{R1} = 0.5$. The eddy viscosity at the wall is now changed from $\tilde{\nu} = 0$ to a non-zero value by using a mixed (Robin) boundary condition at the wall,

$$\frac{\partial \tilde{\nu}}{\partial n} \Big|_{wall} = \frac{\tilde{\nu}_{wall}}{0.03k_s}, \tag{11}$$

where $\frac{\partial \tilde{\nu}}{\partial n}$ is the gradient of $\tilde{\nu}$ in the direction normal to the wall.

3.2. Roughness modification for SST model

The effect of roughness can be accounted for in the $k-\omega$ SST turbulence model by modifying the boundary conditions at the wall as [19].

$$k_{rough} = 0, \tag{12}$$

$$\omega_{rough} = \frac{(\mu_\tau)^2 S_R}{\nu}, \tag{13}$$

where

$$S_R = \begin{cases} \left(\frac{50}{k_s^+}\right)^2, & k_s^+ \leq 25, \\ \left(\frac{100}{k_s^+}\right), & k_s^+ > 25. \end{cases}$$

From equation (5), the eddy viscosity remains zero at the wall, but there is an increase in turbulence dissipation compared to the clean boundary conditions. Here k_{rough} is the turbulent kinetic energy and k_s^+ is the non dimensional equivalent sand grain roughness height.

The two roughness models are implemented in SU2 and are validated below.

4. Model validation

4.1. Turbulent flow over a 2-D flat plate

4.1.1. Grid refinement study

Turbulent flow over a flat plate with different roughness heights is simulated with the SA and the SST turbulence models and their respective roughness corrections presented above. The flat plate domain is 2m long and 1m high and $Re = 6.0 \times 10^6$. A grid refinement study is carried out for the geometry under clean and three roughness levels. There are 57, 113 and 225 points on the surface of the 2-D flat plate for the three grids. The minimum grid spacing is $\Delta y_1 \approx 2 \times 10^{-6}m$. A second set of grids are made with same geometry and same number of points on the surface but with a minimum grid spacing of $\Delta y_2 \approx 3 \times 10^{-8}m$ for the SST roughness model. A growth ratio of 1.09 is used in the normal direction. The skin friction values computed at $x = 0.93m$ are tabulated in Table 1.

Three different roughness heights, $k_s = 1.23 \times 10^{-4}m$, $k_s = 2.46 \times 10^{-4}m$ and $k_s = 9.84 \times 10^{-4}m$ are tested. The k_s^+ values are around 24, 50 and 200 respectively. With a grid spacing of Δy_1 the $y^+ \approx 0.3$ at $x = 0.93$ under clean conditions. As seen in Table 1, a grid independent solution is obtained for the clean case for both the turbulence models with this minimum grid spacing. The SA roughness model gives largely grid independent result for all the roughness heights. However, a grid independent solution is not possible under rough conditions with the SST model. The variation is marginal at low roughness heights and increases as the roughness height increases. With the grid spacing of Δy_2 , grid independent solutions at different roughness heights are obtained with the SST model as well. The y^+ under clean conditions for this grid spacing is 0.006.

The first two roughness heights are in the transitional roughness regime while the third roughness height is in the fully rough regime. The SA roughness modification gives a grid independent solution with a minimum $y^+ \approx 0.3$ whereas the SST roughness model fails to do so in the fully rough regime. This is likely due to how the roughness modification is introduced in the two models. The eddy viscosity at the wall is directly modified in SA but in SST it remains zero. In the fully rough regime, there is a non-zero eddy viscosity in the inner region of the boundary layer where the viscous sub layer previously existed. Since the eddy viscosity is still zero at the wall for the SST roughness modification, to capture the steep increase in eddy viscosity a finer mesh is likely required compared to the SA roughness modification.

4.1.2. Velocity profiles

Despite the finer mesh the skin friction values predicted by the SST roughness model does not match those from the SA model

Table 1

Skin friction (C_f) at $x = 0.93m$ for different grid resolutions and roughness levels with SA and SST. N denotes the number of points on the surface of the flat plate.

$k_s(m)$	N	SA	SST (Δy_1)	SST (Δy_2)
Clean	57	0.00273	0.00267	0.00272
	113	0.00274	0.00271	0.00274
	225	0.00274	0.00273	0.00274
1.23×10^{-4}	57	0.00369	0.00335	0.00346
	113	0.00382	0.00341	0.00346
	225	0.00382	0.00344	0.00346
2.46×10^{-4}	57	0.00451	0.00348	0.00374
	113	0.00457	0.00361	0.00374
	225	0.00457	0.00368	0.00374
9.84×10^{-4}	57	0.00605	0.00375	0.00424
	113	0.00599	0.00392	0.00425
	225	0.00593	0.00413	0.00425

especially under fully rough conditions (Table 1). The velocity profiles in the inner boundary layer are now investigated to determine the accuracy of the two models. The velocity profiles for different roughness heights are presented in Figs. 1 and 2. The profiles are computed based on the grid independent results i.e. with a grid spacing of Δy_1 for SA and Δy_2 for SST. From Figs. 1 and 2, we can see that the clean case matches the viscous sub-layer and log law in the overlap region closely for both the SA and SST models. Further, increasing the equivalent roughness height has the predicted effect of a shift of the velocity profile away from the clean case and once $k_s^+ > 70$, the viscous sub-layer disappears. To further verify the two results, a comparison is made with the empirical shift in velocity profile as proposed by Nikuradse [27] shown below.

$$u^+ = \frac{1}{\kappa} \log\left(\frac{y^+}{k_s^+}\right) + B, \tag{14}$$

where $\kappa = 0.40$ and the shift B is given by

$$\begin{aligned} 1 < k_s^+ < 3.5, B &= 5.5 + \frac{1}{\kappa} \log(k_s^+), \\ 3.5 < k_s^+ < 7, B &= 6.59 + 1.52 \log(k_s^+), \\ 7 < k_s^+ < 14, B &= 9.58, \\ 14 < k_s^+ < 68, B &= 11.5 - 0.7 \log(k_s^+), \\ 68 < k_s^+, B &= 8.48. \end{aligned}$$

Comparing the empirical predictions of the velocity shift (Fig. 1), a slight overprediction is observed in the transitionally rough region by the SA roughness model. This was also reported in Knopp et al. [13]. The SST roughness model does not perform as well as the SA model especially in the fully rough regime (Fig. 2) despite using a much finer grid. The limitations in the $k - \omega$ SST roughness model are also reported elsewhere [13,27,28]. It must be noted that various corrections for the SST roughness model have been proposed (for example [13,27]) but are not investigated in the current study.

4.2. Blanchard experiments

In this section, the two roughness models are compared to the experimental data from Blanchard obtained from Aupoix et al. [22]. The sand grain roughness height was $4.25 \times 10^{-4}m$. With an incoming velocity of $45ms^{-1}$, the simulation is carried out on a $2m$ long flat plate. The resulting Reynolds number is $Re = 6.46 \times 10^6$. The y^+ of the mesh used is less than 0.4 throughout the domain for the SA roughness model and less than 0.007 for the SST roughness

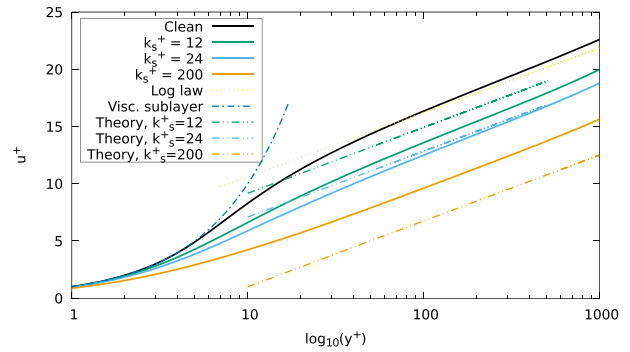


Fig. 2. A comparison of velocity shifts obtained from SST models to the theoretical value.

model. The comparison is shown in Fig. 3. Both the SA and SST models predict a higher skin friction compared to the clean flat plate but the results from the SA roughness model are significantly closer to the experimental data. The resulting $k_s^+ \approx 150$ makes the flow fully rough. As seen in Fig. 2, the SST roughness model performs poorly in this regime which results in an underprediction of the skin friction.

5. Roughness on airfoil sections

Determining the damage caused by erosion on turbine blades is an ongoing field of study. Analytical, numerical and experimental studies [29–31] have been carried out to determine the extent of erosion caused by raindrops. The most widely used approach is the droplet impact model. Eisenberg et al. [30] use analytical methods to determine the extent of erosion damage over time due to raindrops (Fig. 4). The effect of continuous exposure of turbine blades to rain is represented by the cumulative number of rain drop impacts and the material removed because of the impacts are modeled based on experimental research. A review on different approaches to study the erosion caused by weather can be found in Keegan et al. [3].

In this section, the focus will be on validating the roughness models against experimental data where the roughness heights are already determined. To that end, two cases are considered: NACA 64₂215 airfoil at a Reynolds number of $Re = 2.6 \times 10^6$ and the DU-96-W-180 airfoil at a Reynolds number of $Re = 1.85 \times 10^6$. As seen in section 4.1.1, a very fine grid in the wall normal direction is required for the SST roughness model compared to the SA roughness model, which gives grid independent results with meshes comparable to the clean cases. Additionally, despite the fine grid

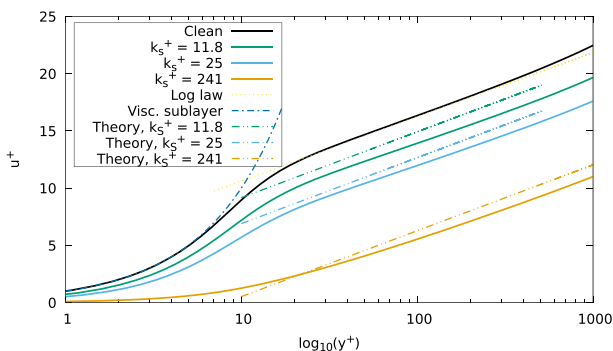


Fig. 1. A comparison of velocity shifts obtained from SA models to the theoretical value.

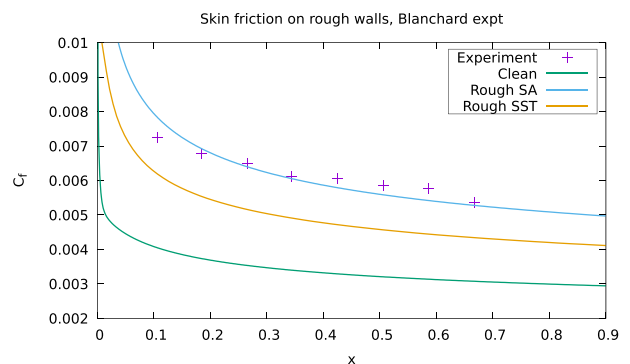


Fig. 3. Comparison of skin friction coefficient (C_f) from SST and SA roughness models to experimental data from Blanchard [22].

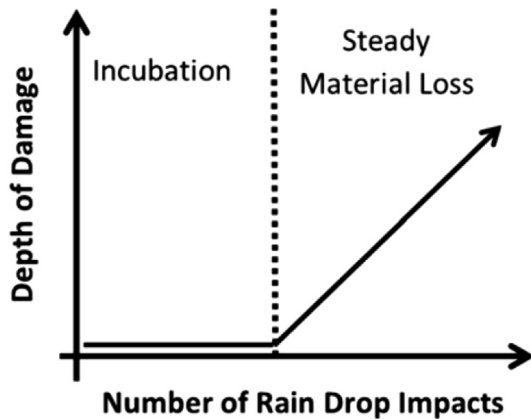


Fig. 4. Surface damage as a function of number of rain drop impacts [30].

the SST roughness model performed poorly compared to the SA roughness model in predicting skin friction for the flat plate. Therefore in the following sections only the SA roughness model will be used. A chord length (c) of $1m$ is assumed and the roughness values are normalized by the chord length.

5.1. NACA 65₂215

In this section the SA model is further validated against the NACA 65₂215 airfoil. The Reynolds number is $Re = 2.6 \times 10^6$ and the roughness covers the entire upper surface and on the lower surface from the leading edge up to $x/c = 0.15$. Three roughness heights $k_s/c = 1.54 \times 10^{-4}$, $k_s/c = 3.08 \times 10^{-4}$ and $k_s/c = 1.23 \times 10^{-3}$ are considered here. Clean experiments were performed by Abbot and von Doenhoff [32]. Ljungstrom performed experiments with different roughness heights on the NACA 65₂A215 airfoil, a closely related airfoil. These experiments have been used to validate roughness models by Knopp [13] and Hellsten [12] previously. The experimental data are also extracted from Knopp and Hellsten.

5.1.1. Grid details

A two dimensional C-grid topology (Fig. 5) is used for all the simulations. A grid refinement study is carried out at an angle of attack of 8° on meshes with 150, 250 and 450 nodes on the airfoil surface. A $y^+ \approx 0.3$ is maintained for the three grids. A growth ratio of 1.09 is used within the boundary layer. The computational domain extends to 150 chord lengths in all directions. The grid is shown in Fig. 6. The resulting lift and drag coefficients are listed in Table 2. Since no appreciable difference is observed between the results on the grids with 250 and 450 points (see Table 2), the grid

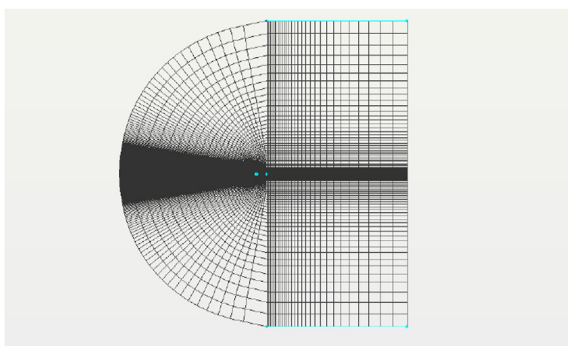


Fig. 5. Grid used for NACA 65₂215 simulations.

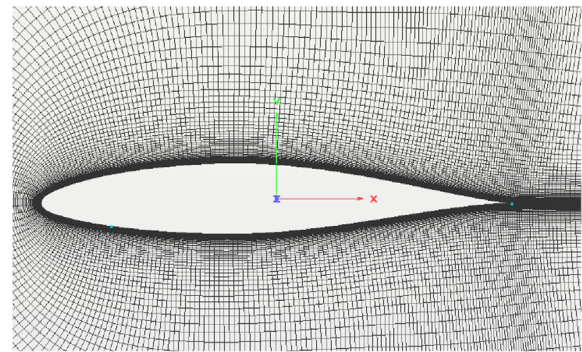


Fig. 6. Grid around NACA 65₂215 airfoil.

Table 2

Lift and Drag coefficients with different grid resolutions for the NACA 65₂215 airfoil.

N	C_l	C_d
150	1.0273	0.0149
250	1.0336	0.0141
450	1.0346	0.0138

with 250 points on the airfoil was used for further computations. The far field and wall boundary conditions are applied at the edge of the domain and on the airfoil respectively.

5.1.2. Clean results

Fig. 7 shows the comparison of the numerical results from the SA model under clean conditions. The results from SU2 compare very well against results from RFOIL [9] and the experiments from Abbot [32] at lower angles of attack, but SU2 overpredicts the maximum lift. This could be due to a later prediction of the flow separation by the SA turbulence model compared to the experiments. Since no experimental pressure data is available, this cannot be confirmed. However, the lift values reported by Ljungstrom are significantly lower. Since the two airfoils under consideration are supposed to be very similar, Hellsten [12] concludes that lift values reported by Ljungstrom are too low likely due to imperfections from a retracted flap in the airfoil geometry setup. The absolute values of the lift coefficients do not compare well against experimental data from Ljungstrom, but considering the comments of Hellsten the absolute lift coefficient values are not comparable either under clean or rough conditions. The maximum lift is

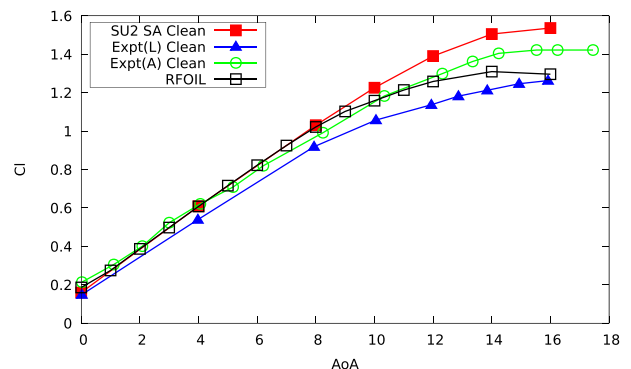


Fig. 7. Comparison of NACA 65₂215 polars against experiments and numerical results from SU2 and RFOIL. Expt(L) refers to results from Ljungstrom and Expt(A) from Abbot and von Doenhoff [32].

observed around an angle of attack of 16° for the clean case in both numerical and experimental data.

5.1.3. Rough results

In Fig. 8 the predicted lift coefficients with different roughness heights are shown. With increasing roughness, the maximum lift value and the angle at which this occurs decrease. Based on the computed skin friction values at an angle of attack of 8°, k_s^+ varies from 70 to about 850. These values suggest the flow is likely to be fully rough but it will vary depending on the flow conditions. As noted earlier, the absolute values of the lift coefficients do not match but the relative drop of lift from SU2 matches closely with the experiments (Table 3). However, SU2 predicts a higher value for the angle at which the maximum lift occurs compared to experiments. This is again likely due to the later prediction of the separation location by the SA model.

5.2. DU 96-W-180

In this section, the SA roughness model is applied to the DU96-W-180 airfoil. DU96-W-180 is an 18% thick airfoil developed by Delft University [33] and is widely used in the wind energy community. Sareen et al. [7] performed experiments on this airfoil at different Reynolds numbers under different stages and types of erosion. Sareen et al. [7] determine the levels of erosion based on photographs of eroded blades. In this study, the leading edge erosion due to pits and gouges (see Fig. 9) under the two most severe stages are considered at $Re = 1.85 \times 10^6$. These cases correspond to Type B stage 3 and stage 4 as reported in Ref. [7].

The depths of pits and gouges are respectively 0.51mm and 2.54mm. The pits and gouges have equal depths and diameters. The chord-wise extent of the pits and gouges are 10% on the upper surface and 13% on the lower surface. The number of pits and gouges on the lower surface is also 1.3 times that on the upper surface. In stage 3 there are 400 pits and 200 gouges on the upper surface and in stage 4 there are 800 pits and 400 gouges on the upper surface.

5.2.1. Grid details

As seen in section 4.1.1, the SA roughness model requires a wall normal grid spacing that corresponds to $y^+ \approx 0.3$ under clean conditions to obtain grid converged results in rough conditions. Thus, this minimum grid spacing is maintained. A grid refinement study is carried out at an angle of attack of 8° with $N = 125, 250, 500$ and 750 points along the airfoil. A growth ratio of 1.09 is used in the normal direction. The resulting lift and drag coefficients are listed in Table 4 along with the fully turbulent results

Table 3
Reduction in maximum lift (%) observed in experiments and SU2 for different roughness heights.

k_s/c	Experiment	SU2
1.54×10^{-4}	14.22	13.38
3.08×10^{-4}	22.20	19.50
1.23×10^{-3}	29.08	30.03

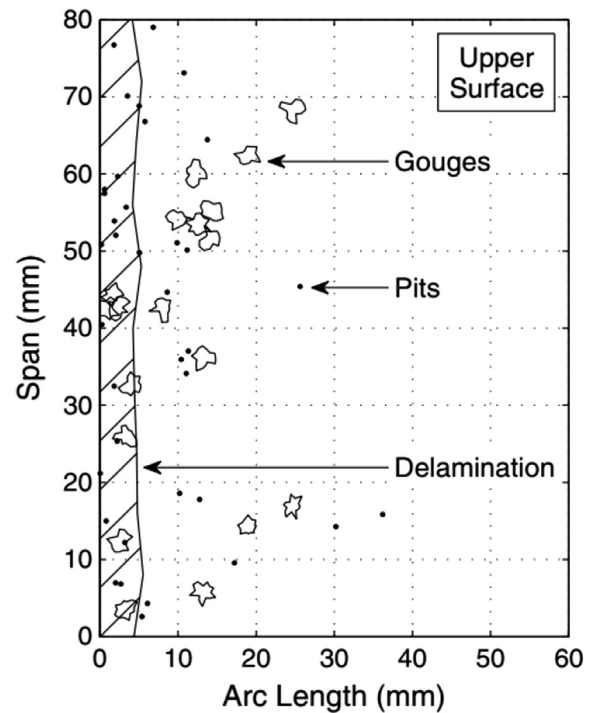


Fig. 9. Illustration of pits, gouges and delamination of a turbine blade from Sareen et al. [7].

obtained from RFOIL [9]. Based on these results the grid with $N = 500$ points on the airfoil is chosen for further analysis.

5.2.2. Clean results

A baseline case of fully turbulent flow is considered before rough simulations. A transition model is not considered since the effect of roughness on transition is not implemented.

Fig. 10 shows the lift coefficient at different angles of attack from SU2 and RFOIL under fully turbulent conditions compared to experimental data. Since no mention of tripping the flow is made in Ref. [7], it is likely that the flow is not fully turbulent but transitional, especially at lower angles of attack. Consequently, a consistent underprediction of lift is observed in both numerical tools. The results from SU2 and RFOIL match closely in the linear region and deviate at higher angles of attack.

Table 4

Lift and Drag coefficients with different grid resolutions for the DU95-W-180 airfoil at an angle of attack of 8°.

N	C_l	C_d
125	1.028934	0.020944
250	1.065950	0.016588
500	1.069648	0.015781
750	1.069287	0.015704
RFOIL	1.054832	0.015551

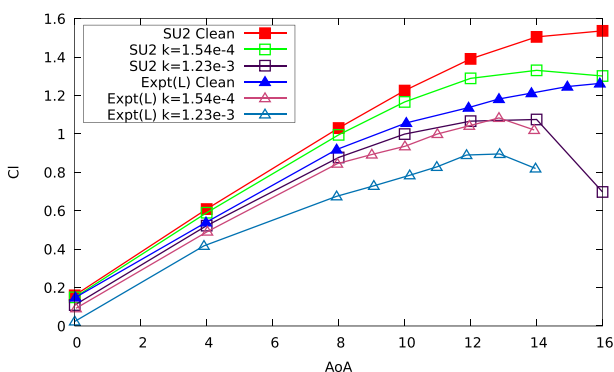


Fig. 8. Comparison of NACA 65₂₁₅ polars against experiments and numerical results with different roughness heights. Expt(L) refers to results from Ljungstrom.

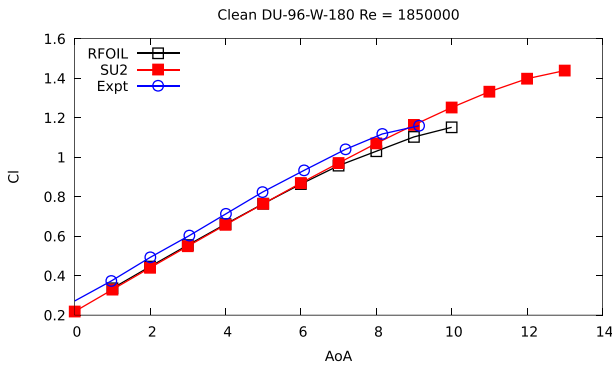


Fig. 10. Comparison of lift coefficient (C_l) against angle of attack for fully turbulent flow against experimental data.

Fig. 11 shows the comparison of lift and drag coefficients of the two numerical results from SU2 and RFOIL with the experimental data. Once again, since the experimental flow conditions were not fully turbulent there is a consistent overprediction of the drag coefficient by both SU2 and RFOIL. As seen in Fig. 10, there is good agreement between the numerical results at lower angles of attack. However, RFOIL predicts increasing flow separation to occur from an $AoA = 9^\circ$, which is close to what is observed in the experiment but is not predicted by SU2. This is likely due to the poor prediction of separation by the SA turbulence model, which was also observed earlier.

5.2.3. Equivalent sand grain roughness

Roughness height, k , is usually defined as the height or depth of roughness elements on the surface, for example, the depth of pits and gouges in Fig. 9. Determination of the equivalent sand grain roughness height, k_s , from the roughness height k is an active area of research. The roughness density parameter, Λ_s , is widely used in literature as a means of relating geometric surface roughness with equivalent sand grain roughness

$$\Lambda_s = \frac{S}{S_f} \left(\frac{A_f}{A_s} \right)^{1.6}, \tag{15}$$

where S is the total wall area where roughness is present, S_f is the roughness frontal area, A_f is the frontal area of a single roughness element, and A_s is the surface area of a single roughness element in the direction of wind flow. Based on data from Schlichting’s experiments, Danberg and Sigal [34] proposed the following relations for 2-D

$$\frac{k_s}{k} = \begin{cases} 3.21 \times 10^{-3} \Lambda_s^{4.935}, & 1.4 \leq \Lambda_s \leq 4.89, \\ 8, & 4.89 \leq \Lambda_s \leq 13.25, \\ 151.71 \Lambda_s^{-1.1379}, & 13.25 \leq \Lambda_s \leq 100, \end{cases} \tag{16}$$

and in 3-D

$$\frac{k_s}{k} = 160.77 \Lambda_s^{-1.3376}, \quad 16 \leq \Lambda_s \leq 200. \tag{17}$$

Van Rij et al. [35] generalized the roughness shape factor A_f/A_s for irregular 3-D roughness elements as S_f/S_w where S_f is the total frontal area of all roughness elements and S_w is the total wetted area of all roughness elements and proposed the following relation

$$\frac{k_s}{k} = \begin{cases} 1.58 \times 10^{-5} \Lambda_s^{5.683}, & \Lambda_s \leq 7.84, \\ 1.802 \Lambda_s^{0.03038}, & 7.84 \leq \Lambda_s \leq 28.12, \\ 255.5 \Lambda_s^{-1.454}, & 28.12 \leq \Lambda_s. \end{cases} \tag{18}$$

McClain [36] used the discrete element method approach and proposed a single relation as

$$\frac{k_s}{k} = 927.317 \Lambda_s^{-1.669}. \tag{19}$$

However, these correlations are mainly derived by adding roughness elements like spheres, cones and hemispheres and their validity for negative roughness like pits and gouges is not clear. Various researchers have used statistical representations of rough surfaces in combination with experiments and numerical simulations using LES and DNS simulations to obtain more general correlations based on rms height (k_{rms}), skewness (Sk) and higher order moments of the rough surface height probability density functions. The k_{rms} and skewness Sk can be computed as

$$k_{rms} = \sqrt{\frac{1}{N} \sum_i k_i^2}, \quad Sk = \frac{1}{N} \sum_i \left(\frac{k_i}{k_{rms}} \right)^3, \tag{20}$$

where k_i are the heights or depths of individual roughness elements, for example a pit, and N is the total number of such roughness elements. Flack and Schultz [37] proposed

$$k_s = 4.43 k_{rms} (1 + Sk)^{1.37} \tag{21}$$

but note that it is not very general since it does not include information about roughness density. In a more recent study, Flack et al. [38] proposed different relations for different types of skewness as

$$k_s = 2.48 k_{rms} (1 + Sk)^{2.24} \tag{22}$$

for positive skewness,

$$k_s = 2.73 k_{rms} (2 + Sk)^{-0.45} \tag{23}$$

for negative skewness and

$$k_s = 2.11 k_{rms} \tag{24}$$

for zero skewness. They also note that negatively skewed surfaces like those with pits and gouges have a smaller impact on drag than positive skewness due to roughness elements. Flack and Schultz [39], and Forooghi et al. [40] also note that another parameter that accounts for sparse roughness is necessary and propose a relation of the form

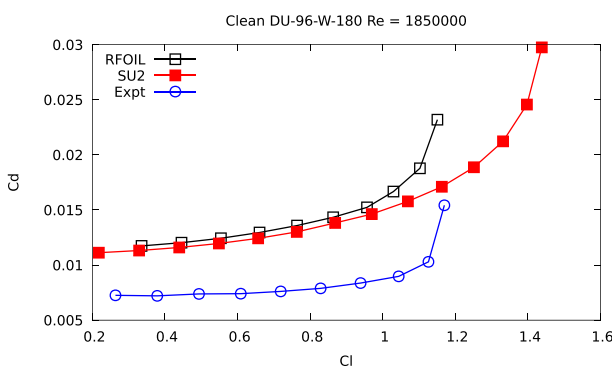


Fig. 11. Comparison of lift coefficient (C_l) against drag coefficient (C_d) for fully turbulent flow against experimental data.

$$k_s / k_z = F(Sk)G(ES), \tag{25}$$

where ES is the effective slope which is related to the solidity of roughness (λ) as $ES = 2\lambda$ and k_z is related to k_{rms} as $k_z = 4.4k_{rms}$. Note that solidity is defined as the ratio of total roughness frontal area (S_f) to total wall area (S). They recommend

$$F(Sk) = 0.67Sk^2 + 0.93Sk + 1.3 \tag{26}$$

and

$$G(ES) = 1.07(1 - e^{-3.5ES}). \tag{27}$$

In this study, equations (25)–(27) suggested by Ref. [40] are used.

5.2.4. Roughness definition

Sareen et al. [7] create different amounts of roughness on the upper and lower surface with the lower surface being 1.3 times rougher than the upper surface. For the type B stage 3 erosion level Sareen et al. add 400 pits and 200 gouges on the upper surface and 520 pits and 260 gouges on the lower surface. In stage 4 the number of pits and gouges are doubled both on the upper and lower surfaces. The rough surface extends from the leading edge to $x/c = 0.1$ on the upper surface and from the leading edge to $x/c = 0.13$ on the lower surface in both cases. The computed statistics are listed in Table 5.

5.2.5. Rough results

Fig. 12 shows the comparison of the lift coefficient as a function of the angle of attack between SU2 and experiments under stage 3 erosion. There is a small underprediction of lift at lower angles of attack, similar to what was observed in the clean case. This is likely due to the flow still being mildly transitional at lower angles of attack. With increasing angle of attack, the prediction from SU2 matches the experimental data quite closely likely due to the flow becoming fully turbulent in the experiment.

Fig. 13 shows the drag and lift coefficients. Once again, the numerical results from SU2 overpredicts the drag compared to the experimental data. Flow separation starts to occur before $AoA \approx 8^\circ$ in the experiments whereas SU2 does not predict separation till after $AoA \approx 9^\circ$.

Fig. 14 shows the comparison of the lift coefficient as a function of the angle of attack between SU2 and experiments under stage 4 erosion. The numerical results agree with the experiments more closely compared to stage 3 likely due to the flow being fully turbulent due to the higher roughness level.

Fig. 15 shows the drag and lift coefficients. Once again, numerical results from SU2 overpredict the drag compared to the experimental data. Flow separation is also predicted better with this extent of erosion compared to stage 3.

Figs. 13 and 15 also show the lift and drag values in clean conditions. The increase in drag even at lower angles of attack can be seen clearly. The maximum lift also decreases in rough conditions for both roughness levels considered. However, since Sareen et al.

Table 5
Roughness definition for DU-96-W-180 based on Sareen et al. [7].

	Stage 3	Stage 4
k_{rms}	1.524mm	1.524mm
Sk	– 1.56695	– 1.56695
ES	0.0563	0.1126
k_s/c	0.00418	0.00760

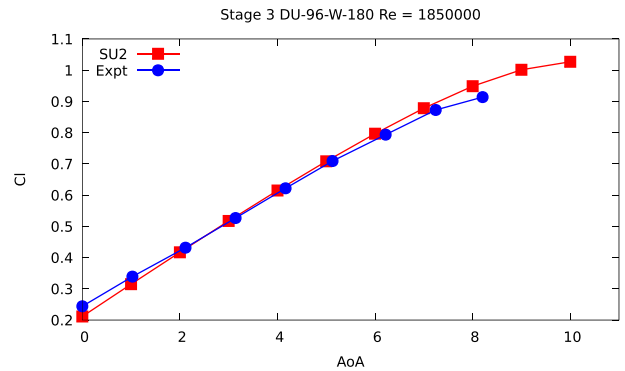


Fig. 12. Comparison of lift coefficient (C_l) against angle of attack for fully turbulent flow against experimental data (stage 3 see Table 5).

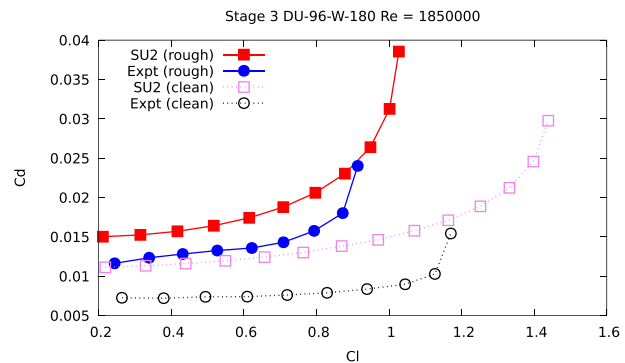


Fig. 13. Comparison of lift coefficient (C_l) against drag coefficient (C_d) for fully turbulent flow against experimental data (stage 3 see Table 5).

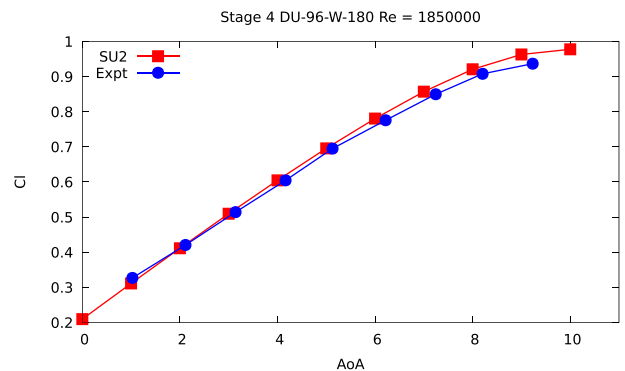


Fig. 14. Comparison of lift coefficient (C_l) against angle of attack for fully turbulent flow against experimental data (stage 4 see Table 5).

[7] do not report lift and drag values at higher angles of attack, the magnitude of reduction cannot be compared. It is very likely that the airfoil will stall earlier for both the roughness cases compared to the clean conditions.

Discussion. In this section the SA roughness model was first validated against experiments on the NACA 65₂215 airfoil with a given equivalent sand grain roughness. The SA model predicted the drop in lift very closely compared to the experiments. Subsequently, the SA model was used on the DU-96-W-180 airfoil with ‘negative’ roughness. It was seen that a statistical description of the surface is required to accurately calculate the equivalent sand grain roughness. Results under clean conditions differed from the experiments likely due to the absence of a transition scheme, but the

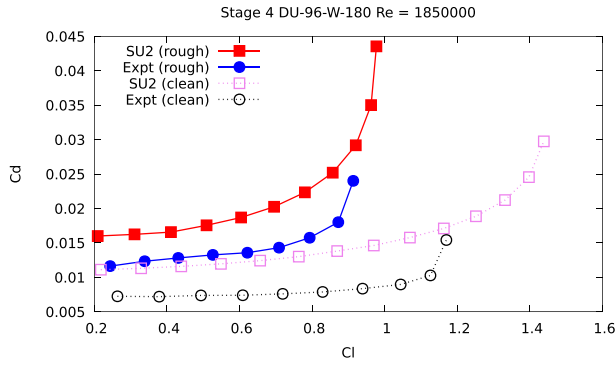


Fig. 15. Comparison of lift coefficient (C_l) against drag coefficient (C_d) for fully turbulent flow against experimental data (stage 4 see Table 5).

numerical results, especially lift coefficient, matched closely with the experimental data under roughness when the flow is likely fully turbulent. It was seen that roughness causes a considerable reduction in lift and increase in drag and can lead to premature stalling of the airfoils.

6. Boundary layer analysis

Since the NACA 65₂215 airfoil has a larger rough surface than the DU-96-W-180, it is chosen for the boundary layer analysis. The boundary layer parameters for SU2 are computed by extracting the velocity vector along surface normals at various points along the airfoil. The edge of the boundary layer is assumed to be at the location where the ratio of the magnitude of the vorticity at that location to the value at the wall is less than 10^{-4} . In this section the effect of roughness on the boundary layer properties of airfoils will be investigated.

6.1. Integral boundary layer methods

The combination of integral boundary layer (IBL) methods with panel methods known as viscous-inviscid interaction (VII) are very commonly used in aerodynamic analysis of airfoils. XFOIL [41] and RFOIL [9] are some of the widely used tools based on this approach. Viscous-inviscid interaction methods give very accurate results at a very low computational cost compared to standard RANS simulations. They are commonly used during the design process of wind turbine blades in combination with blade element momentum (BEM) theory and other rotor design methods. A roughness model for the integral boundary layer methods will allow for a more accurate and quick assessment of the effect of roughness on turbine performance during the design phase.

Integral boundary layer equations are obtained by integrating the boundary layer equations in the direction normal to the wall. More details on deriving the governing equations can be found in Refs. [42,43]. The new integral quantities introduced are displacement thickness δ^* , momentum thickness θ and kinetic energy thickness δ_k .

$$\delta^* = \int_0^\delta \left(1 - \frac{u}{u_e}\right) dy, \quad \theta = \int_0^\delta \frac{u}{u_e} \left(1 - \frac{u}{u_e}\right) dy. \tag{28}$$

$$\delta_k = \int_0^\delta \frac{u}{u_e} \left(1 - \left(\frac{u}{u_e}\right)^2\right) dy,$$

Here u is the local velocity, δ is the boundary layer thickness, u_e

is the velocity magnitude at the edge of the boundary layer and y is the wall normal direction. Further, the following shape parameters are defined

$$H = \frac{\delta^*}{\theta}, \quad H_k = \frac{\delta_k}{\theta}. \tag{29}$$

The governing equations resulting from integration of the continuity and momentum equations used in RFOIL are

$$\frac{d\theta}{dx} + (2 + H - M_e^2) \frac{\theta}{u_e} \frac{du_e}{dx} = C_f / 2, \tag{30}$$

$$\theta \frac{dH_k}{dx} + (2H^{**} + H_k(1 - H)) \frac{\theta}{u_e} \frac{du_e}{dx} = 2C_D - H_k - C_f / 2. \tag{31}$$

Note that other formulations of the integral boundary layer equations are used in other tools [43]. In order to close the equations, closure relations [42,43] are defined for the kinetic energy shape factor H_k , the skin friction coefficient C_f and the dissipation coefficient C_D . The closure relations are different for laminar and turbulent flows. For turbulent flows, an additional equation for lag in Reynolds shear stress (C_τ) is also solved. H^{**} is a shape factor based on the variation of density within the boundary layer and M_e is the Mach number of the external flow. Both can be ignored for incompressible flows. These closure relations are defined in terms of the shape factors introduced earlier and the Reynolds number based on momentum thickness Re_θ , where $Re_\theta = u_e \theta / \nu$ with ν being the kinematic viscosity. In the following sections, the effect of roughness on the different thicknesses, shape factors and closure relations are examined.

6.2. Clean results

First the calculated integral boundary layer quantities from SU2 under clean conditions are compared against the RFOIL results. It must be noted that the X – axis of all the plots in this section range from $x/c = 0.025$ to $x/c = 1$ to avoid the stagnation region. Fig. 16 shows the displacement thickness on both the upper and lower sides at angles of attack of 0° and 4° . The calculated displacement thickness matches closely with the values from RFOIL with some deviation near the trailing edge in both cases.

The momentum thickness is slightly overpredicted by SU2 after $x/c = 0.4$ at an angle of attack of 0° but matches closely for an angle of attack of 4° as seen in Fig. 17.

The comparisons of the shape factors are shown in Fig. 18. The shape factor is larger for $AoA = 4^\circ$ compared to $AoA = 0^\circ$ indicating a thicker boundary layer as the angle of attack increases. While the computed shape factors from RFOIL and SU2 do not match exactly, both display similar behavior initially decreasing towards the middle of the airfoil and increasing near the trailing edge.

In RFOIL [9] the local skin friction coefficient is computed as [42].

$$C_f = \frac{0.3 \exp(-1.33H)}{(\log_{10} Re_\theta)^{1.74 + 0.31H}} + \tag{32}$$

$$0.00011 \left(\tanh \left(4.0 - \frac{H}{0.875} \right) - 1.0 \right).$$

Here Re_θ is the local Reynolds number based on momentum thickness θ . Fig. 19 shows the comparison of the skin friction coefficient between RFOIL, the values reported by SU2 originally by the RANS computation (denoted as ‘SU2 original’) and the skin friction calculated based on the computed integral boundary layer

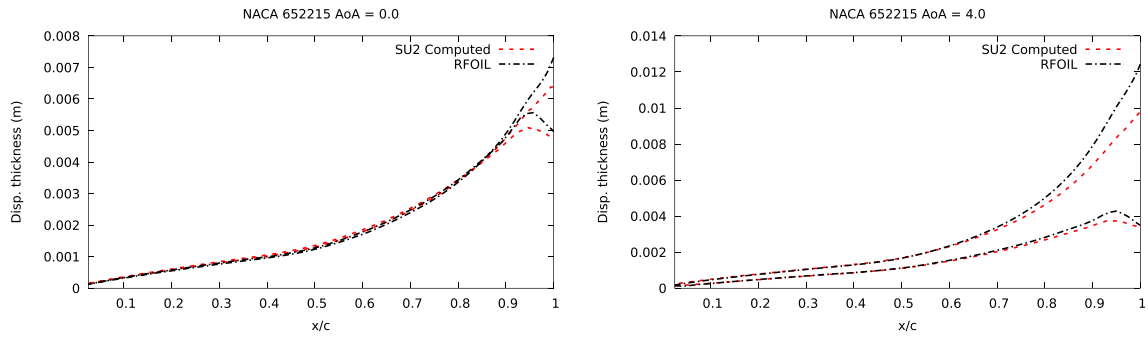


Fig. 16. Displacement thickness (δ^*) from SU2 and RFOIL at an angle of attack of 0° (top) and 4° (bottom) for the NACA 65₂215 airfoil.

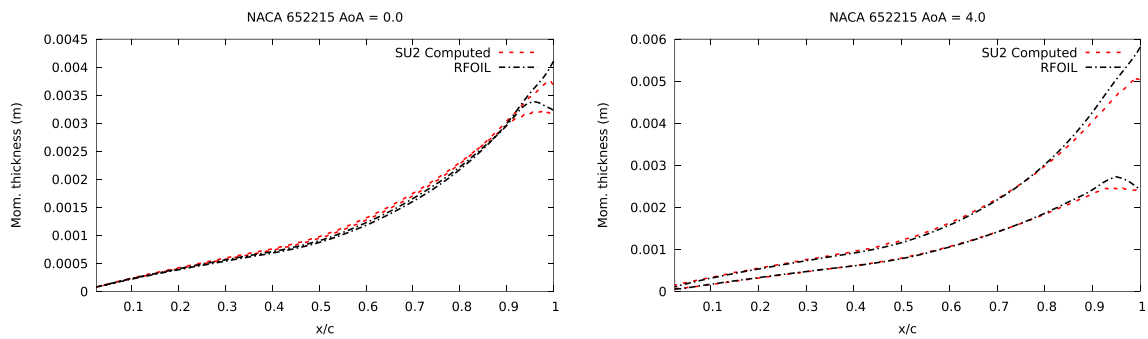


Fig. 17. Momentum thickness (θ) from SU2 and RFOIL at an angle of attack of 0° (top) and 4° (bottom) for the NACA 65₂215 airfoil.

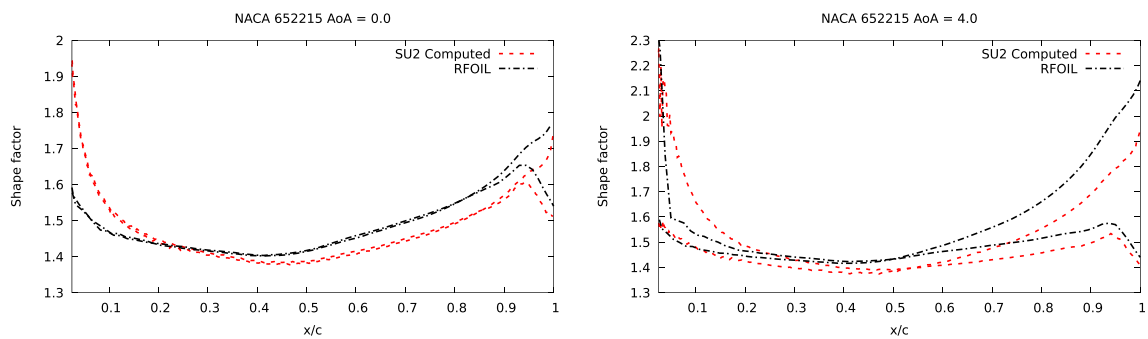


Fig. 18. Shape factor (H) from SU2 and RFOIL at an angle of attack of 0° (top) and 4° (bottom) for the NACA 65₂215 airfoil.

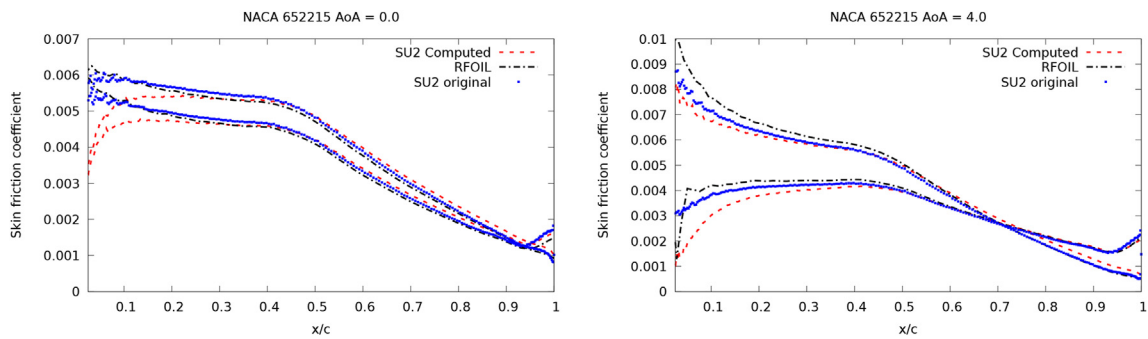


Fig. 19. Skin friction coefficient (C_f) from SU2 and RFOIL at an angle of attack of 0° (top) and 4° (bottom) for the NACA 65₂215 airfoil.

quantities in equation (32) (denoted as ‘SU2 Computed’). The C_f computed from the integral quantities using equation (32) match the SU2 RANS solution and RFOIL results quite well after $x/c = 0.25$. The mismatch near the leading edge for $AoA = 0^\circ$ is likely due

to errors in computing the integral quantities near the stagnation region.

6.3. Rough results

Since the entire upper surface is rough the results for the upper surface only are presented in this section. Figs. 20 and 21 shows the displacement and momentum thickness for different roughness levels compared to the clean case. As expected, these thicknesses increase with increasing roughness. A very steep increase is observed in the momentum thickness near the trailing edge for the largest roughness.

Fig. 22 shows the shape factors for different roughness levels compared to the clean case at $AoA = 0^\circ$ and $AoA = 4^\circ$. The shape factor increases for all roughness levels with the largest increase for $k_s = 1.23 \times 10^{-3}$. The maximum k_s^+ values varies with angle of attack. At an angle of attack of 0° , the k_s^+ are 25, 75 and 286 indicating that the flow is in the transitional rough region for the two lower roughness levels and is fully rough for the highest roughness level. However, at an angle of attack of 4° , the maximum k_s^+ values are 75, 180 and 750 indicating that the flow is fully rough for the $k_s/c = 3.08 \times 10^{-4}$ case also. From Fig. 22 it is seen that the behavior of the shape factor in the $k_s/c = 3.08 \times 10^{-4}$ case is similar for both angles of attack despite one being transitionally rough and the other fully rough.

6.3.1. Skin friction coefficient

Equation (32) will not be valid here as the properties of the boundary layer change due to roughness. Olsen et al. [10] suggested a new closure relation for skin friction for rough surfaces including the Reynolds number based on roughness height, $Re_k = u_e k / \nu$ as

$$C_f = \frac{0.9 \exp(-2.4H)}{(\log_{10} Re_\theta - \log_{10} Re_k + 1.11)^{2.45 - 0.15H}} \quad (33)$$

Fig. 23 shows the skin friction from equations (32) and (33), clean and rough SU2 results at angles of attack of 0° (top) and 4° (bottom). Clearly equation (32) is not valid for rough surfaces. The new closure relation proposed by Olsen et al. appears to overpredict the skin friction. However, since the computed Re_k for the first two roughness levels are approximately 400 and 800, it is outside the range of the data used by the authors in their study. The third roughness level has an average $Re_k \approx 3000$ and is within the valid range of data used to derive the model. The authors report convergence difficulties when roughness was applied to regions before $x/c = 0.6$ and from Fig. 23 it can be seen that C_f is over-predicted by a significant amount in that region and is closer to the values reported by SU2 after $x/c = 0.6$.

6.3.2. Kinetic energy shape factor

As seen above the closure sets for skin friction are not valid for rough airfoils. The other closure relation defined in terms of H and

Re_θ is for the kinetic energy shape factor H_k . Closure relations for other quantities are defined in terms of C_f and H_k . Thus, the validity of the H_k closure is examined here in detail. For turbulent flows in RFOIL the following closure relations are used to compute H_k . First define

$$H_0 = \begin{cases} 3.0 + \frac{400}{Re_\theta}, & Re_\theta > 400, \\ 4.0 & Re_\theta \leq 400. \end{cases} \quad (34)$$

Then for $H < H_0$

$$H_k = \left(0.5 - \frac{4.0}{Re_\theta}\right) \left(\frac{H_0 - H}{H_0 - 1}\right)^2 \frac{1.5}{H + 0.5} + 1.5 + \frac{4}{Re_\theta}, \quad (35)$$

otherwise

$$H_k = 1.5 + \frac{4.0}{Re_\theta} + (H - H_0)^2 \left[\frac{0.04}{Re_\theta} + 0.007 \frac{\ln Re_\theta}{\left(H - H_0 + \frac{4}{Re_\theta}\right)^2} \right] \quad (36)$$

The computed H_k based on equation (29) (denoted by symbols) and those based on the closure relations in equations (35) and (36) (denoted by solid lines) are shown in Fig. 24. The computed values agree with the closure relations closely for the clean case and also for the two lowest roughness cases. However, as the level of roughness increases the closure relation does not predict H_k accurately. The Re_k of the first two roughness cases are approximately 400 and 800, indicating that the closure sets are likely valid for small roughness levels but deviate for higher roughness levels. The deviation observed in the third roughness level is also much less than the deviation observed for the skin friction coefficient. Fig. 25 shows the variation of H_k for a higher angle of attack of 12° . From the top figure it is seen that the behavior of H_k is similar to that observed for lower angles of attack when the flow is attached. However, as the bottom figure shows, the deviation increases for all roughness levels when the flow separates. The wiggles observed are likely an artefact of how the edge of the boundary layer is detected during the post processing.

Since the closure relations for the dissipation coefficient (C_D) and for turbulent flows the Reynolds shear stress coefficient (C_τ) are based on H , Re_θ , C_f and H_k , all of which change with roughness, new closure relations need to be defined. Thus, in order to model roughness in integral boundary layer method based tools like RFOIL, new closure relations need to be derived for all of the above quantities.

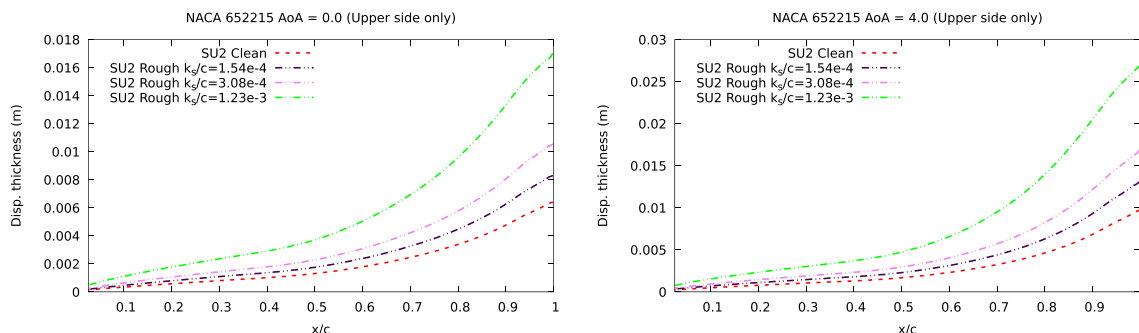


Fig. 20. Displacement thickness (δ^*) from SU2 under different roughness levels at an angle of attack of 0° (top) and 4° (bottom) for the NACA 65,215 airfoil.

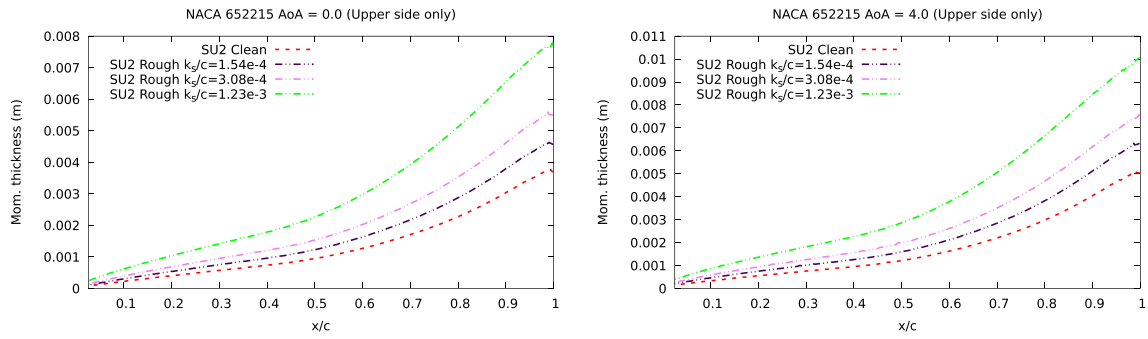


Fig. 21. Momentum thickness (θ) from SU2 under different roughness levels at an angle of attack of 0° (top) and 4° (bottom) for the NACA 65₂215 airfoil.

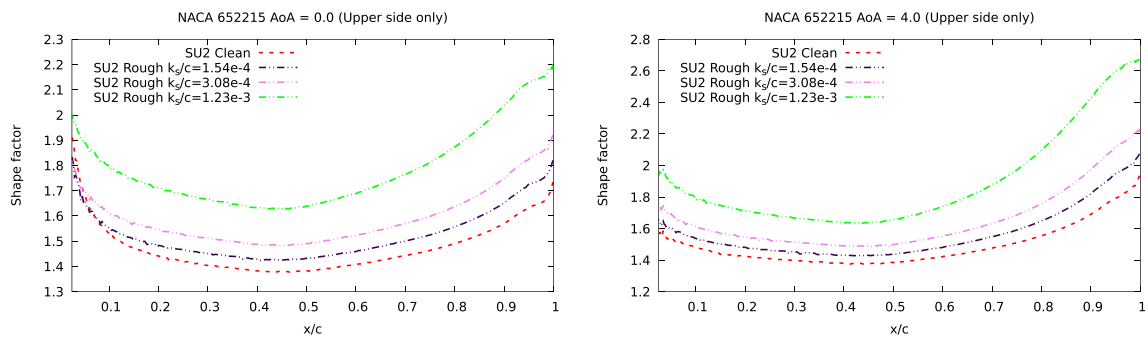


Fig. 22. Shape factor (H) from SU2 under different roughness levels at an angle of attack of 0° (top) and 4° (bottom) for the NACA 65₂215 airfoil.

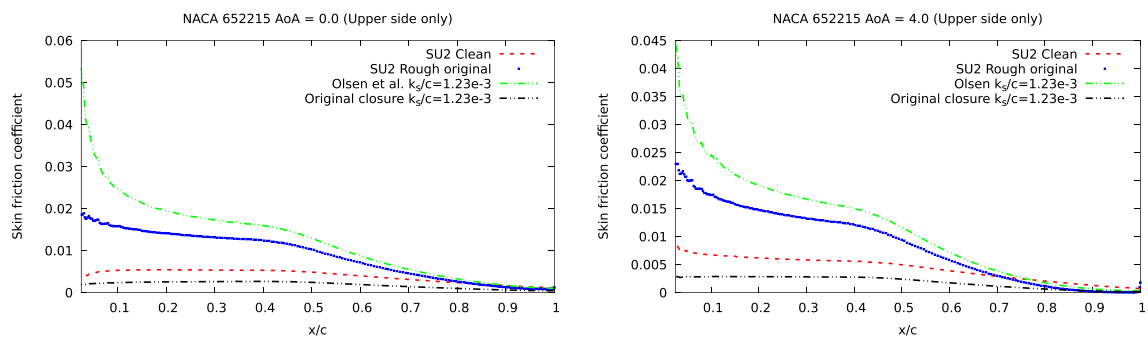


Fig. 23. Skin friction coefficient (C_f) comparison between RANS solution from SU2 (clean in red and rough in blue) and closure relations from Olsen et al. [10] and RFOIL [9] at an angle of attack of 0° (top) and 4° (bottom) for the NACA 65₂215 airfoil.

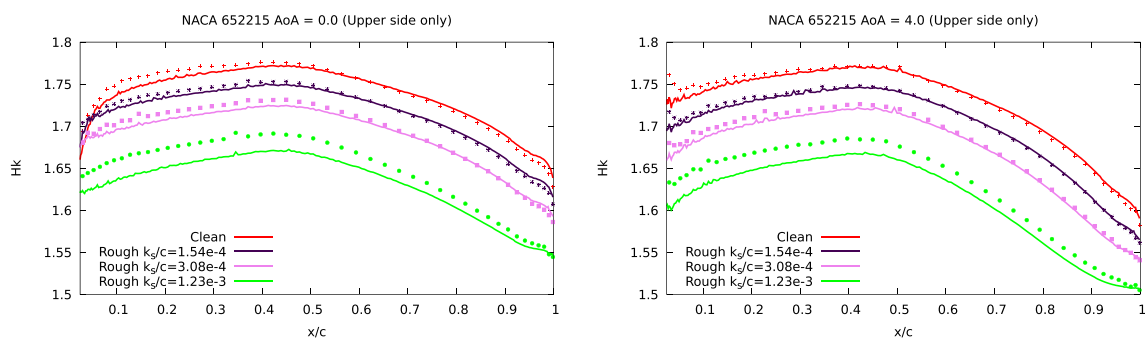


Fig. 24. H_k from SU2 under different roughness levels at an angle of attack of 0° (top) and 4° (bottom) for the NACA 65₂215 airfoil. Computed values (equation (29)) shown as symbols and result from the closure relations (equations (35) and (36)) as solid lines.

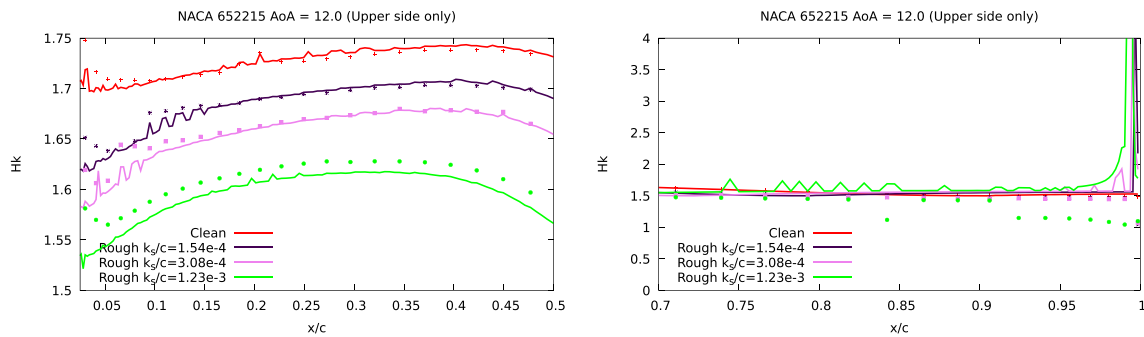


Fig. 25. H_k from SU2 under different roughness levels at an angle of attack of 12° for the NACA 652215 airfoil. Top figure shows the plot from $x/c = 0.025$ to $x/c = 0.5$. Bottom figure shows the zoomed in region around the TE for all roughness levels. Computed values (equation (29)) shown as symbols and result from the closure relations (equations (35) and (36)) as solid lines.

6.4. Discussion

In this section, the different integral boundary layer quantities and closure relations used in RFOIL are examined under clean and rough conditions. Three different roughness levels were considered corresponding to Re_{k_s} of approximately 400, 800 and 3000. The boundary layer thicknesses increase due to roughness and the shape factor is also higher. A larger shape factor typically implies a thicker boundary layer that is prone to separation. The shape factor remained less than 2 for the lower two roughness levels but for the highest roughness level the shape factor neared the value for separation even at low angles of attack. Additionally, it was seen that the variation of the shape factor followed the variation of Re_{k_s} more closely than the variation of k_s^+ . Closure relations are crucial for an accurate solution in integral boundary layer methods. The performance of the closures for skin friction and kinetic energy shape factor was examined under rough conditions. The closure relation for skin friction underperformed significantly for all cases. The new closure relation proposed by Olsen et al. [10] was observed to overpredict the skin friction. The kinetic energy shape factor closure relation was less sensitive to roughness and showed significant deviation only for the largest roughness case and separated flow.

7. Conclusions and future outlook

Leading edge erosion causes a reduction in aerodynamic performance of wind turbine blades. Depending upon the extent of roughness, a drop in maximum lift of up to 30% can be observed. Skin friction increase was observed in all cases leading to an increase in drag. Effect of roughness is modeled using the equivalent sand grain roughness height. Roughness models for the two RANS turbulence models SA and SST were implemented in SU2 and the accuracy was examined via grid refinement. The models were validated against empirical models for the shift in velocity profiles in the boundary layer and experimental skin friction data on flat plates. It was seen that the SST roughness model required a much finer grid compared to the SA roughness model to give a grid independent solution. However, despite the finer grid the results from the SST roughness model did not match the experimental data or the empirical models under fully rough conditions, unlike the SA roughness model. Based on these results the SA roughness model was further validated against experimental data on two different airfoils. The SA model predicted the reduction in lift for different roughness levels accurately for the NACA 652215 airfoil. The SA model was also validated against an experiment with negative roughness (pits and gouges) on the DU-96-W-180 airfoil.

Encouraging results were observed for both roughness levels tested. The statistical method to determine the equivalent sand grain roughness proved to be accurate. Some differences were observed in the clean simulation, most likely due to the fact the simulations were run under fully turbulent conditions, unlike the experiments.

Further, the behavior of different integral boundary layer properties like displacement thickness, momentum thickness, shape factors and closures were investigated for the NACA 652215 airfoil. The existing skin friction closure relations for clean surfaces greatly underpredict the skin friction (C_f) and are not valid for rough surfaces. However, the closure relation for the kinetic energy shape factor (H_k) performed well for low roughness levels ($Re_{k_s} < 1000$) but deviated at higher roughness levels and under separation. The deviation was only marginal compared to the skin friction closure relation. However, since the closure relations for other quantities like the dissipation coefficient and the Reynolds shear stress coefficient depend on C_f and H_k new closure relations will be needed in order to simulate rough surfaces in integral boundary layer tools like RFOIL.

The main focus of this study was on the effect of roughness on turbulent boundary layers. For laminar boundary layers, roughness leads to premature transition and for turbulent boundary layers. In order to fully capture the effect of roughness, the effect on transition will also be considered in the future. Further, more boundary layer data at different roughness levels are needed to derive new closure relations for integral boundary layer methods.

CRedit authorship contribution statement

Akshay Koodly Ravishankara: Conceptualization, Software, Methodology, Validation, Investigation, Formal analysis, Writing – original draft. **Huseyin Özdemir:** Conceptualization, Methodology, Supervision, Validation, Writing – review & editing, Data curation. **Edwin van der Weide:** Conceptualization, Methodology, Supervision, Writing – review & editing.

Declaration of competing interest

The authors declare that they have no known competing financial interests or personal relationships that could have appeared to influence the work reported in this paper.

References

- [1] R. Herring, K. Dyer, F. Martin, C. Ward, The increasing importance of leading edge erosion and a review of existing protection solutions, *Renew. Sustain. Energy Rev.* 115 (2019) 109382.
- [2] W. Han, J. Kim, B. Kim, Effects of contamination and erosion at the leading

- edge of blade tip airfoils on the annual energy production of wind turbines, *Renew. Energy* 115 (2018) 817–823.
- [3] M.H. Keegan, D. Nash, M. Stack, On erosion issues associated with the leading edge of wind turbine blades, *J. Phys. Appl. Phys.* 46 (38) (2013) 383001.
 - [4] R.S. Ehrmann, B. Wilcox, E.B. White, D.C. Maniaci, Effect of surface roughness on wind turbine performance, in: *Tech. Rep., Sandia National Lab.(SNL-NM), Albuquerque, NM (United States)*, 2017.
 - [5] C.M. Langel, R. Chow, C. Van Dam, D.C. Maniaci, Rans based methodology for predicting the influence of leading edge erosion on airfoil performance. *Tech. Rep., Sandia National Lab.(SNL-NM), Albuquerque, NM (United States)*, 2017.
 - [6] F. Menter, R. Langtry, S. Völker, Transition modelling for general purpose cfd codes, *Flow, turbulence and combustion* 77 (1–4) (2006) 277–303.
 - [7] A. Sareen, C.A. Sapre, M.S. Selig, Effects of leading edge erosion on wind turbine blade performance, *Wind Energy* 17 (10) (2014) 1531–1542.
 - [8] J. Nikuradse, et al., *Laws of Flow in Rough Pipes*, 1950.
 - [9] R. Van Rooij, Modification of the Boundary Layer Calculation in Rfoil for Improved Airfoil Stall Prediction, Sep 1996.
 - [10] A.S. Olsen, N. Ramos-García, C. Bak, Improved roughness model for turbulent flow in 2d viscous-inviscid panel methods, *Wind Energy* 23 (3) (2020) 608–616.
 - [11] F. Palacios, S. Padron, B. Tracey, D.E. Manosalvas, A. Aranake, S.R. Copeland, A. Variyar, J.J. Alonso, T.W. Lukaczyk, A.K. Lonkar, K.R. Naik, T.D. Economon, Stanford University Unstructured (SU2, Analysis and Design Technology for Turbulent Flows (January), 2014, pp. 1–33.
 - [12] A. Hellsten, S. Laine, A. Hellsten, S. Laine, Extension of the k-omega-sst turbulence model for flows over rough surfaces. 22nd Atmospheric Flight Mechanics Conference, 1997, p. 3577.
 - [13] T. Knopp, B. Eisfeld, J.B. Calvo, A new extension for k-omega turbulence models to account for wall roughness, *Int. J. Heat Fluid Flow* 30 (1) (2009) 54–65.
 - [14] T.D. Economon, Simulation and adjoint-based design for variable density incompressible flows with heat transfer, *AIAA J.* (2019) 1–13.
 - [15] A. Koodly Ravishankara, H. Ozdemir, E. van der Weide, Implementation of a pressure based incompressible flow solver in su2 for wind turbine applications. *AIAA Scitech 2020 Forum*, 2020, p. 992.
 - [16] P. Spalart, S. Allmaras, A one-equation turbulence model for aerodynamic flows. 30th Aerospace Sciences Meeting and Exhibit, 1992, p. 439.
 - [17] D.C. Wilcox, et al., *Turbulence Modeling for CFD*, vol. 2, DCW industries La Canada, CA, 1998.
 - [18] P. Spalart, Trends in Turbulence Treatments, in: *Fluids 2000 Conference and Exhibit*, p. 2306.
 - [19] D.C. Wilcox, Turbulence modeling for cfd. la canada, ca, Dcw industries, Inc, November, 2006.
 - [20] S.B. Pope, *Turbulent Flows*, Cambridge University Press, 2000.
 - [21] H. Schlichting, K. Gersten, *Boundary-layer Theory*, Springer, 2016.
 - [22] B. Aupoix, P. Spalart, Extensions of the spalart-allmaras turbulence model to account for wall roughness, *Int. J. Heat Fluid Flow* 24 (4) (2003) 454–462.
 - [23] A.L. Braslow, E.C. Knox, Simplified Method for Determination of Critical Height of Distributed Roughness Particles for Boundary-Layer Transition at Mach Numbers from 0 to 5, 1958.
 - [24] R. Dirling Jr., A method for computing roughwall heat transfer rates on reentry nosetips. 8th Thermophysics Conference, 1973, p. 763.
 - [25] R. Grabow, C. White, Surface roughness effects nosetip ablation characteristics, *AIAA J.* 13 (5) (1975) 605–609.
 - [26] C.M. Langel, R. Chow, C.P.v. Dam, M.A. Rumsey, D.C. Maniaci, R.S. Ehrmann, E.B. White, A Computational Approach to Simulating the Effects of Realistic Surface Roughness on Boundary Layer Transition, 52nd Aerospace Sciences Meeting, 2014.
 - [27] B. Aupoix, Roughness corrections for the k-omega shear stress transport model: status and proposals, *J. Fluid Eng.* 137 (2) (2015).
 - [28] B. Aupoix, Wall roughness modelling with k-w STT model, in: 10th International ERCOFTAC Symposium on Engineering Turbulence Modelling and Measurements, Marbella, Spain, 2014.
 - [29] H. Kirols, M. Mahdipoor, D. Kevorkov, A. Uihlein, M. Medraj, Energy based approach for understanding water droplet erosion, *Mater. Des.* 104 (2016) 76–86.
 - [30] D. Eisenberg, S. Laustsen, J. Stege, Wind turbine blade coating leading edge rain erosion model: development and validation, *Wind Energy* 21 (10) (2018) 942–951.
 - [31] A. Castorriani, A. Corsini, F. Rispoli, P. Venturini, K. Takizawa, T.E. Tezduyar, Computational analysis of wind-turbine blade rain erosion, *Comput. Fluids* 141 (2016) 175–183 (advances in Fluid-Structure Interaction).
 - [32] I.H. Abbott, A.E. Von Doenhoff, *Theory of Wing Sections: Including a Summary of Airfoil Data*, Courier Corporation, 2012.
 - [33] W. Timmer, R. Van Rooij, Summary of the delft university wind turbine dedicated airfoils, *J. Sol. Energy Eng.* 125 (4) (2003) 488–496.
 - [34] J.E. Danberg, A. Sigal, Analysis of turbulent boundary-layer over rough surfaces with application to projectile aerodynamics, in: *Tech. Rep., Army Ballistic Research Lab Aberdeen Proving Ground MD*, 1988.
 - [35] J.A. Van Rij, B. Belnap, P. Ligrani, Analysis and experiments on three-dimensional, irregular surface roughness, *J. Fluid Eng.* 124 (3) (2002) 671–677.
 - [36] S.T. McClain, S.P. Collins, B.K. Hodge, J.P. Bons, The importance of the mean elevation in predicting skin friction for flow over closely packed surface roughness, *J. Fluid Eng.* 128 (3) (2005) 579–586.
 - [37] K.A. Flack, M.P. Schultz, Roughness effects on wall-bounded turbulent flows, *Phys. Fluids* 26 (10) (2014) 101305.
 - [38] K. Flack, M. Schultz, J. Barros, Skin friction measurements of systematically-varied roughness: probing the role of roughness amplitude and skewness, *Flow, Turbulence and Combustion* 104 (2) (2020) 317–329.
 - [39] K.A. Flack, M.P. Schultz, Review of hydraulic roughness scales in the fully rough regime, *J. Fluid Eng.* 132 (4) (2010).
 - [40] P. Forooghi, A. Stroh, F. Magagnato, S. Jakirlić, B. Frohnappfel, Toward a universal roughness correlation, *J. Fluid Eng.* 139 (12) (2017).
 - [41] M. Drela, Xfoil: an analysis and design system for low Reynolds number airfoils, in: *Low Reynolds Number Aerodynamics*, Springer, 1989, pp. 1–12.
 - [42] M. Drela, Two-dimensional transonic aerodynamic design and analysis using the euler equations, in: *Tech. Rep., Gas Turbine Laboratory, Massachusetts Institute of, Cambridge, Mass*, 1986.
 - [43] H. Özdemir, *Interacting Boundary Layer Methods and Applications*, Springer International Publishing, Cham, 2020, pp. 1–53.